Steric hindrance induced low exciton binding energy enables low-driving-force organic solar cells

N.B. When citing this work, cite the original published paper.

(article starts on next page)

Aggregate WILEY

RESEARCH ARTICLE

Steric hindrance induced low exciton binding energy enables low-driving-force organic solar cells

Tianyu Hu[1] [ID] | **Xufan Zheng[1]** | **Ting Wang[1]** | **Aziz Saparbaev[2]** | **Bowen Gao[3]** | **Jingnan Wu[4]** | **Jingyi Xiong[3]** | **Ming Wan[1]** | **Tingting Cong[1]** | **Yuda Li[3]** | **Ergang Wang[4]** | **Xunchang Wang[1]** | **Renqiang Yang[1]**

[1]Key Laboratory of Optoelectronic Chemical Materials and Devices (Ministry of Education), School of Optoelectronic Materials & Technology, Jianghan University, Wuhan, China

[2]Institute of Ion-Plasma and Laser Technologies, National University of Uzbekistan, Tashkent, Uzbekistan

[3]Key Laboratory of Novel Biomass-Based Environmental and Energy Materials in Petroleum and Chemical Industry, Key Laboratory for Green Process of Ministry of Education, School of Chemical Engineering and Pharmacy, Wuhan Institute of Technology, Wuhan, China

[4]Department of Chemistry and Chemical Engineering, Chalmers University of Technology, Göteborg, Sweden

Correspondence
Xunchang Wang and Renqiang Yang, Key Laboratory of Optoelectronic Chemical Materials and Devices (Ministry of Education), School of Optoelectronic Materials & Technology, Jianghan University, Wuhan 430056, China.
Email: wangxc@jhun.edu.cn and yangrq@jhun.edu.cn

Abstract
Exciton binding energy (E_b) has been regarded as a critical parameter in charge separation during photovoltaic conversion. Minimizing the E_b of the photovoltaic materials can facilitate the exciton dissociation in low-driving force organic solar cells (OSCs) and thus improve the power conversion efficiency (PCE); nevertheless, diminishing the E_b with deliberate design principles remains a significant challenge. Herein, bulky side chain as steric hindrance structure was inserted into Y-series acceptors to minimize the E_b by modulating the intra- and intermolecular interaction. Theoretical and experimental results indicate that steric hindrance-induced optimal intra- and intermolecular interaction can enhance molecular polarizability, promote electronic orbital overlap between molecules, and facilitate delocalized charge transfer pathways, thereby resulting in a low E_b. The conspicuously reduced E_b obtained in Y-ChC5 with pinpoint steric hindrance modulation can minimize the detrimental effects on exciton dissociation in low-driving-force OSCs, achieving a remarkable PCE of 19.1% with over 95% internal quantum efficiency. Our study provides a new molecular design rationale to reduce the E_b.

KEYWORDS
exciton binding energy, exciton dissociation, organic solar cells, steric hindrance

1 | INTRODUCTION

Organic solar cells (OSCs) are one of the promising technologies for the realization of low-cost solar energy conversion due to their attractive properties of light weight, mechanical flexibility, and roll-to-roll processability method.[1–4] Currently, state-of-art OSCs are constructed with a bulk heterojunction (BHJ) architecture, with the electron donor (D) and electron acceptor (A) constructing a bi-continuous inter-penetrating D/A network structure.[5–9] One of crucial steps in obtaining a high yield of free charge carriers in BHJ systems is hole/electron transfer at the organic/inorganic heterointerface through the interfacial energy offsets between D and A as driving forces.[10–13] However, compared to inorganic and perovskite solar cells, OSCs experience an extra voltage loss due to the need for interfacial driving

force to promote fast and efficient charge separation and generation,[14–26] which limits further improvements in the power conversion of OSCs.

In fact, the minimum driving force required for OSCs is highly dependent on the structural characteristics of the photovoltaic materials. For OSCs using fullerene derivatives as the acceptor, effective charge generation typically necessitates a minimum interfacial energy offset exceeding 0.3 eV, imposing significant limitations on power conversion efficiencies (PCEs) to around 11%.[11,27,28] In recent years, with the development of A–D–A structured nonfullerene acceptors (NFAs), particularly Y6 series molecular system featured strong near-infrared absorption approaching 930 nm, and small or even near-zero interfacial energy offset in the highest occupied molecular orbital (HOMO) level demanded for efficient dissociation of excitons on NFAs, the performances of OSCs have dramatically reach over 19% for the single-junction devices.[29–34] Nevertheless, there remains a lack of comprehensive understanding regarding how to minimize the needed driving force for exciton dissociation in OSCs.

Generally, there is a direct relationship between the needed driving force and E_b for photovoltaic materials.[25,35–38] Different from free charges in inorganic semiconductors, photogenerated electrons and holes are generally bound as localized excitons due to the low dielectric constants of organic photoactive materials.[39,40] If the E_b is higher, the required driving force to dissociate the excitons will also increase accordingly, and thus, more energy is needed to drive localized exciton separation to form free charges.[25,38] In other word, the demand of interfacial driving forces for exciton dissociation in OSCs is mainly ascribed to the strong E_b in organic active materials.[41] Among previous reports focusing on lowing the E_b by molecular design, Cui et al. tailored the main chain of SMAs by using DBTPT unit, and a decrease in E_b was observed due to its inherent backbone rigidity, molecular planarity, and strong electron delocalization.[42] Jen et al. found that introducing an asymmetric structure with selenium substitution resulted in an elevated dielectric constant of SMA, consequently lowering the E_b.[43] Chen's team illustrated that the bromine on SMAs' central unit greatly controls the molecular packing and intermolecular interactions, resulting in better molecular crystalline ordering, increased relative dielectric constant, and ultimately a notable reduction in E_b was obtained.[44] Steric hindrance effect is also a commonly used approach in molecular design and is expected to have an impact on E_b.[45] The steric hindrance effect arises from the spatial constraints within a molecule, limiting the freedom of molecular motion and interaction, which can potentially affect the electronic structure and distribution of electron clouds, thereby influencing the formation and binding energy of excitons.[46] However, there is still lacking fundamental study on how to precisely utilize the steric hindrance effect at the molecular level to finely control the binding energy, ensuring rapid exciton dissociation and charge transfer to enable efficient OSCs.

In this work, we report a molecular design strategy aimed at modulating the E_b of the acceptor by introducing the steric hindrance via precisely tailored side chain. In brief, two isomeric Y6 derivatives, named Y-C5Ch and Y-ChC5 (Figure 1A), by replacing n-hexyl with cyclohexyl at positions proximal and distal to the main skeleton have been

designed for investigation. A combination of experimental and theoretical studies provides physical insights to reveal the relationship between intra/intermolecular interaction, E_b, and the photovoltaic performance of three acceptors. The significant steric hindrance caused by the bulky side chain in Y-ChC5 induces molecular distortion and modest reduction in intramolecular interactions (the interaction forces between atoms), thereby limiting the molecule's rotational freedom. Conversely, this steric hindrance approach enhances intermolecular interactions, leading to a compact molecular stacking pattern. This alteration in molecular interactions can enhance molecular polarizability, promote greater electronic orbital overlap between molecules, and facilitate delocalized charge transfer pathways, ultimately resulting in a decreased E_b. Consequently, the Y-ChC5 exhibited the lowest E_b value compared to the other two counterparts, which was further confirmed by temperature-dependent photoluminescence (PL) measurement. In addition, transient absorption (TA) spectroscopy data show that the charge separation dynamics of PM6:Y-ChC5 were ultrafast, with highest hole transfer efficiency of 95.6%. This leads to a high-efficiency low-driving-force OSC (19.1%) with a J_{sc} of 26.8 mA cm^{-2}, a V_{oc} of 0.897 V, and an FF of 0.794. Overall, this study contributes a new molecular design rationale to minimize E_b by modulating steric hindrance.

2 | RESULTS AND DISCUSSION

Figure 1A shows the molecular structures of Y6, Y-C5Ch, and Y-ChC5, and the detailed synthesis procedures for the newly designed Y-C5Ch and Y-ChC5 featuring cyclohexyl side chain at inner and outer positions of main skeleton are described in Supporting Information Section. The chemical structures of the intermediates and final products were definitively characterized using ^{1}H NMR, ^{13}C NMR, and mass spectrometry (Schemes S1 and S2 and Figures S27–S47). For our design, the isomerism engineering of flexible side chains is expected to achieve NFAs with precisely controlled steric hindrance (large for Y-ChC5, medium for Y-C5Ch, and small for Y6), facilitating investigation into the correlation between intra- and intermolecular interactions and exciton binding energies.

The ultraviolet–visible light absorption of Y6, Y-C5Ch, and Y-ChC5 in solution exhibits remarkable similarity due to their same conjugated backbones (Figure S1). In the solid state, Y-ChC5 displays a broader absorption spectrum and slightly larger optical bandgaps compared to Y6 and Y-C5Ch (Figure 1B). This disparity may be ascribed to alterations in intra- and intermolecular interactions resulting from steric hindrance effect.[47] The electrochemical cyclic voltammetry measurement (Figure 1C, Figure S2, and Table S1) indicates that the steric hindrance effect has minimal impact on the HOMO and lowest unoccupied molecular orbital (LUMO) energy levels of Y6, Y-C5Ch, and Y-ChC5. The relative alignment of HOMO and LUMO levels is consistent with the results obtained from ultraviolet photoelectron spectroscopy measurement and density functional theory (DFT) calculation (Figures S3 and S4). The differential scanning calorimetry analysis revealed exothermal peaks at temperatures of 295.7, 323.1, and 330.6°C for Y6, Y-C5Ch, and Y-ChC5, respectively (Figure S5). The different melting enthalpies (ΔH_m)
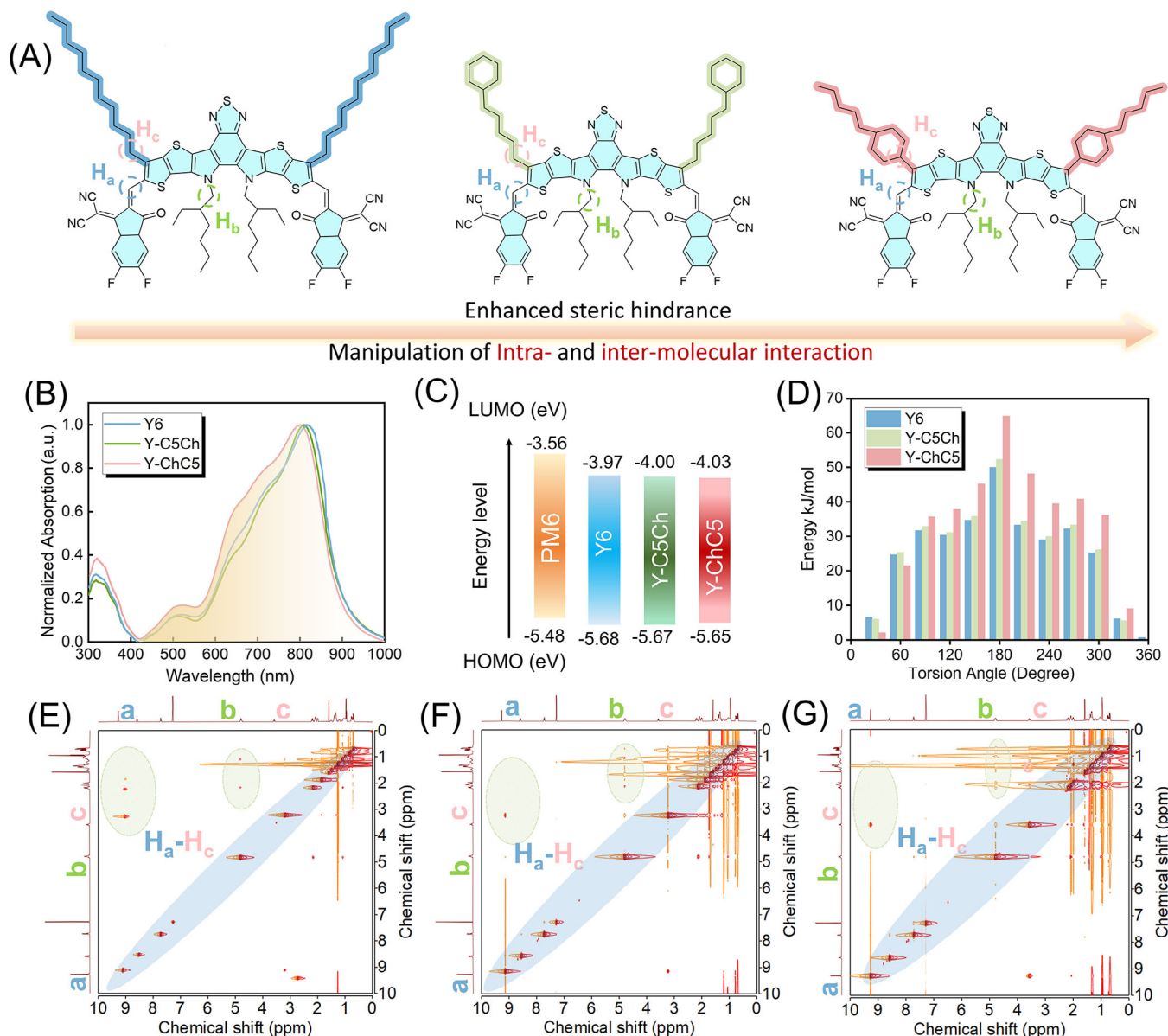
FIGURE 1 (A) Molecular structures of Y6, Y-C5Ch, and Y-ChC5. (B) Normalized ultraviolet–visible (UV–vis) absorption spectra of neat films. (C) Energy diagram of the three nonfullerene acceptors (NFAs) determined by cyclic voltammetry (CV) measurements. (D) Relaxed potential energy scans of the subunits of the three NFAs. Full-range ^1H–^1H Nuclear Overhauser Effect Spectroscopy (NOESY) two-dimensional (2D) NMR spectra of (E) Y6, (F) Y-C5Ch, and (G) Y-ChC5. HOMO, highest occupied molecular orbital; LUMO, lowest unoccupied molecular orbital.

of Y6 (34.80 J g^{-1}), Y-C5Ch (41.90 J g^{-1}), and Y-ChC5 (47.06 J g^{-1}) imply that the presence of a bulky cyclohexyl chain has a significant impact on molecular interaction and aggregation properties. In addition, through relaxed potential energy scans simulation for the torsion axis between the thieno[3,2-*b*]thiophene and the end group, we found that the 180° conformation of Y-ChC5 exhibits ~20 kJ mol^{-1} higher energy than that of Y6 (Figure 1D and Figure S6). This observation indicates that the cyclohexyl close to the main skeleton generates higher rotational barrier for the end group, in turn verifying the strong steric hindrance effect in Y-ChC5.[48]

The two-dimensional (2D) ^1H–^1H Nuclear Overhauser Effect Spectroscopy (NOESY) NMR spectra reveal observed NOE correlation signals only between protons within a distance of up to 5 Å, which allows for the investigation of molecular interactions and, in particular, the spatial relationships between different molecules.[49] In comparison to the ^1H–^1H NOESY spectra of pure Y6 in CDCl$_3$ solution

(Figure 1E), the off-diagonal signals (Figure 1G, green-dashed box), associated with the end groups and sidechains attached to pyrrole ring of the core (H$_a$–H$_c$), were significantly diminished in the spectra of Y-ChC5. A similar trend was also observed for the altered off-diagonal signals in Y-ChC5, likely corresponding to the correlation of protons (H$_b$–H$_c$, H$_b$–H$_b$), suggesting a reduction in intramolecular interaction in Y-ChC5 due to the presence of significant steric hindrance.[50] In addition, another noteworthy discrepancy is the broadest cross-correlation resonance peak which was observed on the diagonal for Y-ChC5 among the three NFAs, indicating the strongest intermolecular interaction of adjacent Y-ChC5 molecules.[51] Analysis of the Fourier transform infrared spectroscopy (FTIR) measurements revealed that the symmetrical and asymmetrical stretching vibrations of the –CH$_2$ BT units in Y-ChC5 occur at 2851 and 2919 cm^{-1}, respectively, which are lower than those of Y-C5Ch (2855 and 2922 cm^{-1}) and Y6 (2857 and 2925 cm^{-1}) (Figure S7). The blue-shifted phenomenon in the FTIR measurement
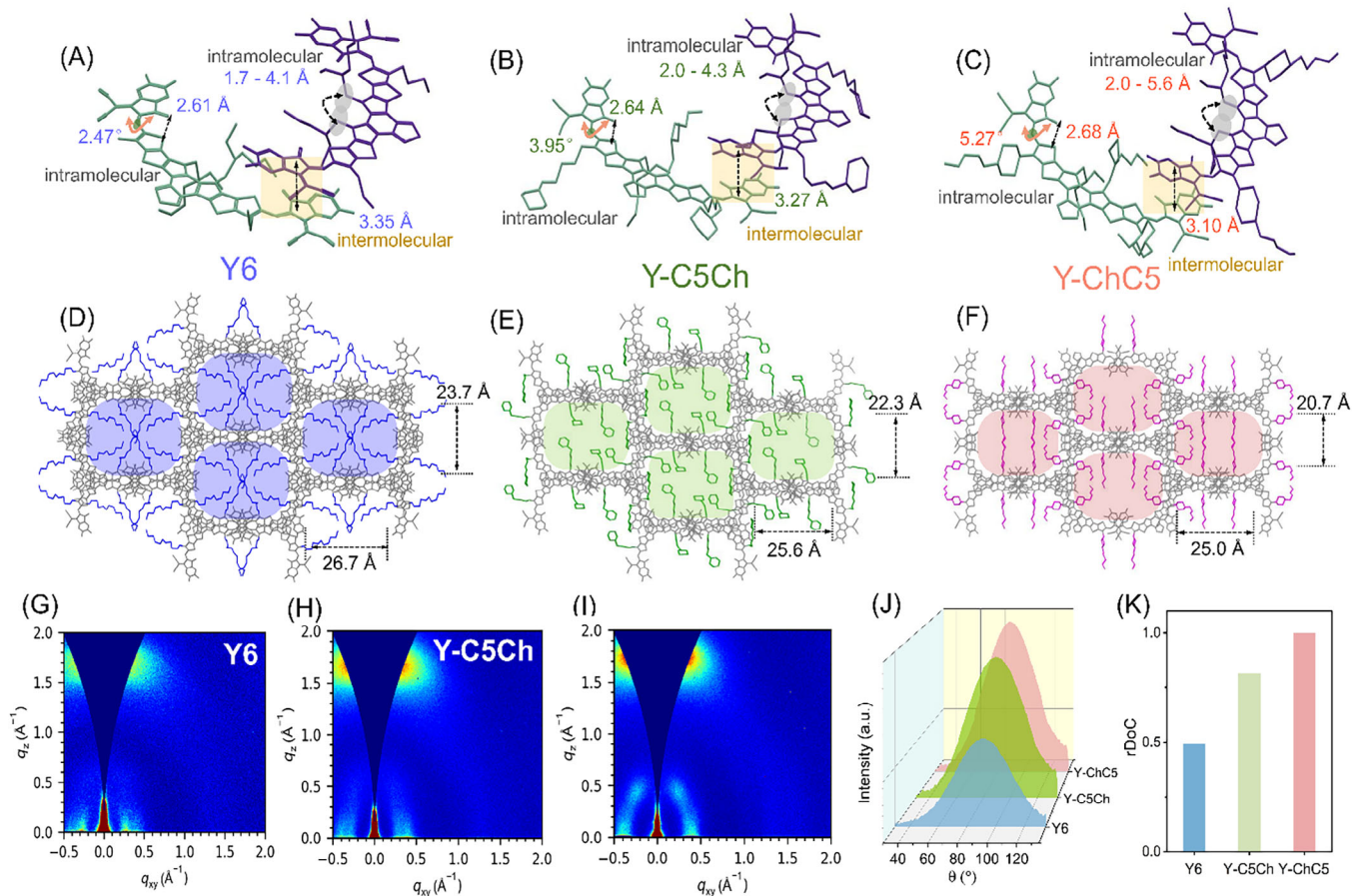
FIGURE 2 Single-crystal structures of (A) Y6, (B) Y-C5Ch, and (C) Y-ChC5. Crystal interpenetrating network packing of (D) Y6, (E) Y-C5Ch, (F) Y-ChC5. Two-dimensional (2D) GIWAXS patterns of (G) Y6, (H) Y-C5Ch, (I) Y-ChC5 pristine films. (J) Pole figures calculated from the (0 1 0) π–π stacking peak. (K) Relative degree of crystallinity of the three neat films obtained by integrating the pole figures.

consistently confirmed the strongest intermolecular interaction in Y-ChC5.

To understand how the steric hindrance affects structural and intra/intermolecular interaction information, single crystals were prepared via the diffusion method and analyzed by single-crystal X-ray diffraction (XRD), and corresponding crystallographic data are presented in Table S9. From the overall view in Figure 2A–C, all three crystals can be classified as triclinic systems with two types of inequivalent molecules per unit cell (refined as A and B), and favorable three-dimensional molecular packing networks established. The dihedral angles between the central core and the end groups of Y-C5Ch and Y-ChC5 are 3.95° and 5.27°, which were slightly larger than that of Y6 (2.47°). Thus, the distance between O atom at end groups and S atom at the periphery of donor unit increases from 2.61 Å for Y6 to 2.64 Å for Y-C5Ch, and further to 2.68 Å for Y-ChC5. This indicates that the enhanced steric hindrance for Y-ChC5 at side chain position can weaken intramolecular noncovalent interactions to slightly distort the molecular skeleton.[46] The weakened intramolecular interaction between the aromatic and aliphatic group of Y-ChC5 can be further corroborated by the intramolecular interaction between the –NCH$_2$– groups that are attached to the aromatic core, as evidenced by Y-ChC5 displaying the smallest average distance value between two –NCH$_2$– groups. On the contrary, packing models reveal that Y-ChC5 adopts a grid-like arrangement in which each Y-ChC5 molecule engages in cofacial π–π interactions (3.10 Å)

within each layer, exhibiting a tighter packing compared to Y6 (3.35 Å) and Y-C5Ch (3.27 Å) (Figure S8). This observation implies that introducing bulkier yet shorter side chains may contribute to a reduced probability of interlayer molecular stacking disruption, thereby promoting a more condensed π–π stacking of the molecules.[48,52]

Moreover, alterations in steric hindrance of the side chain result in varying void sizes. The data presented in Figure 2D–F illustrate that augmenting steric hindrance in proximity to the main skeleton notably decreases lateral distances and increases vertical distances. The packing coefficients for Y6 and Y-C5Ch are 54.5% and 58.7%, respectively, with a higher value observed for Y-ChC5 (64.2%). Consequently, Y-ChC5 molecules exhibit a denser molecular packing and stronger molecular interactions. The grazing incidence XRD results further confirmed varying molecular packing arrangements and crystallinity among three acceptors, with Y-ChC5 molecules exhibiting the most uniform and tightly packed face-on π–π stacking (Figure 2G–I, Figure S9, and Table S2). The relative degrees of crystallinity values for the pure films calculated based on (0 1 0) diffraction peak intensity were 0.49, 0.81, and 1.0 for Y6, Y-C5Ch, and Y-ChC5, implying strongest crystallinity and intermolecular interaction in Y-ChC5 film (Figure 2J,K).[53] These results are also consistent with the variation in neat film electron mobility (Figure S10 and Table S3), where higher electron mobility of Y-ChC5 (3.51×10^3 cm^2 V^{-1} s^{-1}) was obtained in comparison with that of Y6 and Y-C5Ch (1.03×10^3 and
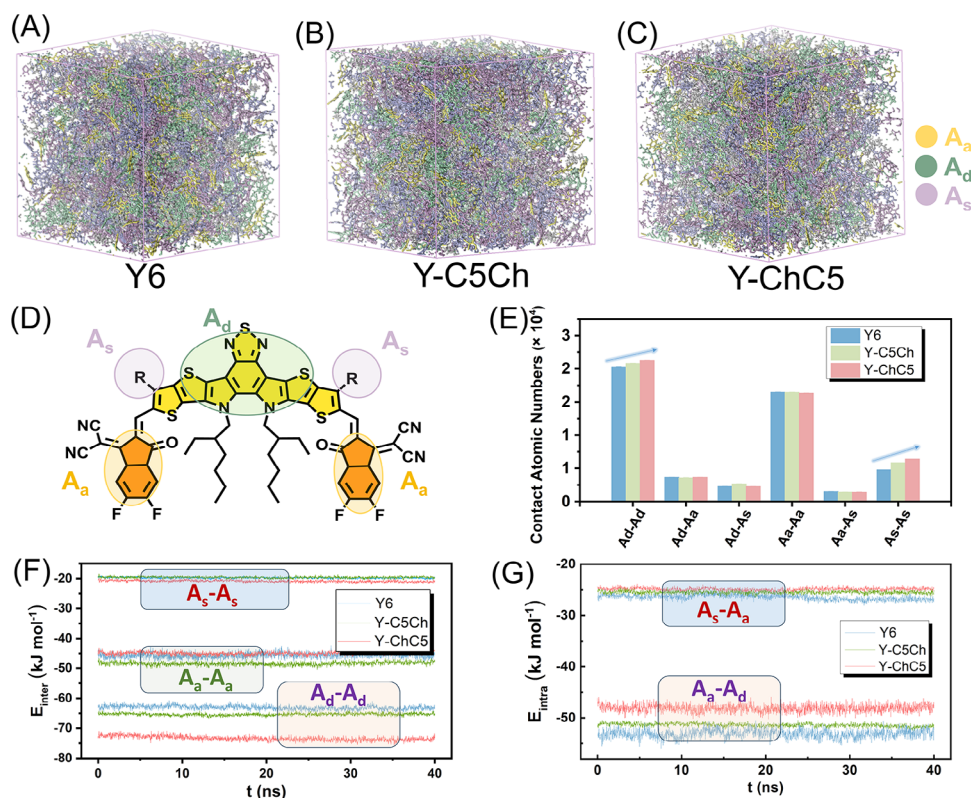
FIGURE 3 Representative snapshot of molecular packing morphology of the simulated (A) Y6, (B) Y-C5Ch, and (C) Y-ChC5 thin films. (D) The clarification of the A_a, A_d, and A_s fragment for all acceptors (taking Y6 as an example). (E) The number of close contacts between the acceptor fragments in the molecular dynamics (MD) simulation system. (F) The intermolecular interaction energy of Y6, Y-C5Ch, and Y-ChC5. (G) The intramolecular interaction energy of Y6, Y-C5Ch, and Y-ChC5.

1.79×10^3 cm^2 V^{-1} s^{-1}). Consequently, the increased steric hindrance in Y-ChC5 molecules relative to Y6 and Y-C5Ch molecules may result in a slight decrease in intramolecular interactions but a notable increase in intermolecular interactions, which could impact the distribution of charges and the binding energy of excitons.[54–56]

To further validate the impact of steric hindrance on inter- and intramolecular interactions for the three acceptors, we applied atomistic molecular dynamics simulations to provide information from both structural and energetic aspects. PM6 was selected as the polymer donor to construct the BHJ system to demonstrate the true spatial state of molecular interactions. Figure 3A–C illustrates the three simulation systems, each consisting of 15 PM6 octamers and 90 acceptor molecules. In addition, the molecular structures of acceptors were categorized into three parts (Figure 3D): side chains (A_s), backbone (A_d), and end groups (A_a), and corresponding inter- and intramolecular interaction energies (E_{intra} and E_{inter}: the sum of electrostatic force and van der Waals force) are displayed in Figure 3F,G. Atoms are considered to be interacting when the interatomic distances are smaller than the sum of their atomic van der Waals radii.[41] The high numbers of atoms involved in A_d–A_d and A_s–A_s interactions, as well as the strongest E_{inter}, exhibited by Y-ChC5 suggest its propensity for forming tightly ordered π–π stacking, consistent with the smallest void size observed in single-crystal measurement (Figure 3E and Table S4).[57] Such compact 2D brick-layer arrangement could generate more pure domains for superior charge transport channels, contributing to suppressed charge recombination and improved

FF for high performance in device.[56] Therefore, it can be inferred that decreasing the longitudinal length of the side chains and increasing steric hindrance with the main skeleton can potentially improve intermolecular interactions for Y-series acceptors. Additionally, compared with the E_{intra} values (the sum of A_s–A_a and A_a–A_d) of −86.7 and −82.1 kJ mol^{-1} for Y6 and Y-C5Ch, Y-ChC5 generates the weakest intramolecular interaction among the three acceptor systems ($E_{intra} = -72.4$ kJ mol^{-1}); thus, the introduction of steric hindrance using bulky side chains can regulate molecular interaction, leading to alterations in electron cloud distribution and subsequently impacting the polarization energy and E_b of acceptors.[10]

Then, we estimate the E_b for the three acceptors. E_b is defined as the energy difference between the transport gap (E_g^t) and the optical gap (E_g^o), where E_g^t can be calculated by subtracting the electron affinity (EA) from the ionization potential (IP) and E_g^o refers to the excitation energy of the first singlet excited state. The molecules in gas phase for the three acceptors were first calculated according to the DFT and time-dependent DFT method, and corresponding results are collected in Table S5. The alterations in geometric structures lead to slight variations in the values of IP, EA, and energy gap (E_g^o) for the three acceptors, with the calculated E_b values of 1.57, 1.56, and 1.53 eV for Y6, Y-C5Ch, and Y-ChC5, respectively (Figure 4B). This indicates that the large steric hindrance via incorporation of bulky side chain in Y6-series molecules could slightly weaken the E_b value in gas phase. Nevertheless, such large E_b values for all three acceptors indicate that excitons are impossible to dissociate in the gas phase.[35,58,59]
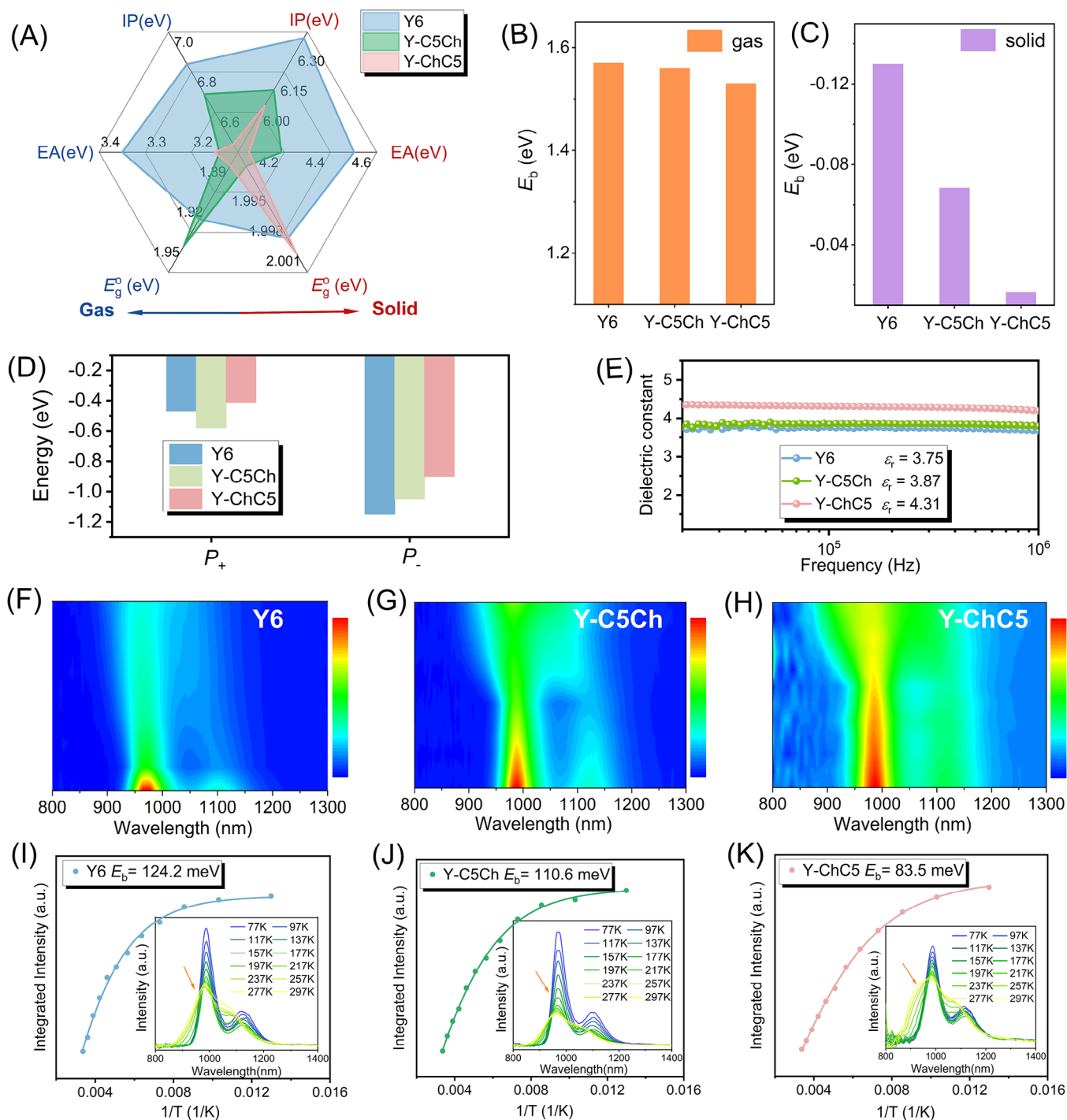
FIGURE 4 (A) Calculated ionization potential (IP), electron affinity (EA), optical gap (E_g^o) for Y6, Y-C5Ch, and Y-ChC5 in gas phase and solid phase. (B) Calculated E_b for Y6, Y-C5Ch, and Y-ChC5 in gas phase. (C) Calculated E_b for Y6, Y-C5Ch, and Y-ChC5 in solid phase. (D) Polarization energies and the corresponding electrostatic and induction components for the positive and negative charges. (E) Relative dielectric constant as a function of frequency measured by impedance spectroscopy. The temperature-dependent photoluminescence (PL) spectra of (F) Y6, (G) Y-C5Ch, and (H) Y-ChC5 neat films. Integrated PL emission intensity as a function of temperature (inset: temperature-dependent PL spectra, $\lambda_{excitation}$ = 750 nm) of (I) Y6, (J) Y-C5Ch, and (K) Y-ChC5 neat films.

Subsequently, E_b of three different molecules with different geometry structures in the solid phase was calculated using the self-consistent quantum mechanics/embedded charge method, taking into account the polarization effects, including both electrostatic and induction interactions (Figures S11 and S12).[59] Due to the similarity in electrostatic potentials for three acceptors, both the first singlet excited state (S$_1$) and the ground state (S$_0$) exhibit almost identical stabilization energies (Figures S13 and S14). Consequently, the change in E_g^o from the gas phase to the solid phase is extremely small and can be considered negligible. In contrast, the stabilization energies of the three molecules undergo significant changes, resulting in notable variations in their IP and EA energies, with the IP/EA values of 6.37/4.50, 6.11/4.19, and 6.03/4.05 eV for Y6, Y-C5Ch, and Y-ChC5, respectively (Figure 4A). Correspondingly, the E_b shows a progressive decrease as the steric hindrance effect strengthens, decreasing from −0.130 eV (Y6) to −0.071 eV (Y-C5Ch) and further declining to −0.016 eV (Y-ChC5) (Figure 4C).

It is well-established that in the solid phase, the complex and tightly packed arrangement of the main skeleton can lead to a pronounced and stable charge-carrier polarization effect, compared to neutral excitons, which significantly impacts the E_b of the molecule.[60] Thus, the electronic polarization energy (P^+/P^-) of charge carrier (positive or negative) is estimated and partitioned into electrostatic (P_{elst}) and induction (P_{ind}) components: $P = P_{elst} + P_{ind}$.[58] P_{elst} arises from the Coulomb interaction between the permanent charges of the molecule and its neighboring molecules (as derived from the electron density in the gas phase), and P_{ind} originates from the induced charge redistribution among all the molecules. The obtained polarization energies, electrostatic contributions, and induction contributions for the three acceptors are displayed in Figure 4D. The P_{elst} values of the three molecules are similar, whereas a notable disparity is observed in the P_{ind} values. The increase in P_{ind} from −1.0 eV (Y6) to −1.2 eV (Y-C5Ch) and subsequently to −1.6 eV (Y-ChC5) may primarily stem from the changed inter- and intramolecular interaction induced by the steric hindrance, which in turn affect the electron cloud distribution. The differences in polarizability among the three acceptors in the solid state can also be verified by the analysis of relative dielectric constant (ε_r).[61] Figure 4E displays the ε_r of the pristine films as measured by impedance spectroscopy. In comparison to the neat films Y6 ($\varepsilon_r = 3.75$) and Y-C5Ch ($\varepsilon_r = 3.87$), the Y-ChC5 film exhibited a higher value of 4.31. Considering the similar conjugation structure of the three acceptors but different packing models, it is hypothesized that alterations in inter- and intramolecular interactions may play a significant role in enhancing molecular polarizability. The analysis indicates a strong linear correlation between the electronic polarization energy (P^+/P^-) and the E_b in the solid state, with Y-ChC5 exhibiting a lower E_b compared to the other two molecules.

Furthermore, we employed temperature-dependent PL spectra measurements from 77 to 297 K to further confirm the variation of E_b for three molecules, and the data are summarized in Figure 4F–K. At room temperature, two excitonic peaks are distinguished from the deconvolved Gaussian fitting ($R^2 = 0.999$), with one sharp peak at 1.28 eV (~970 nm) corresponding to the main 0–0 transition and another peak at 1.10 eV (~1120 nm) corresponding to the shoulder 0–1 transition (Figure S15). As the temperature decreases, the integrated PL peak intensity increases monotonically, allowing for the experimental determination of E_b by fitting the data using the Arrhenius equation: $I(T) = I_0/(1 + A \exp(-E_b/k_B T))$, where I_0 is the intensity at 0 K, k_B is the Boltzmann constant, and T is the temperature.[62] Accordingly, the E_b of Y6 is derived as 124.2 meV, and due to its slightly twisty main skeleton and larger packing density, leading to a more delocalized charge transfer pathway, Y-C5Ch exhibits a much lower E_b of 110.6 meV. The E_b further decreases to 83.5 meV (for Y-ChC5) by introducing bulky cyclohexane to regulate the inter- and intramolecular interaction. Here, we should note that for the typical Y6 film, Chen and coworkers have reported a similar temperature-dependent trend that aligns with the findings of this study,[44] whereas Wei and Yi et al. have observed an opposite variational trend of temperature-dependent PL intensity.[41] As the change in PL intensity, especially in low temperatures, of the photovoltaic material is very complex, the construction of physical models may not be perfect. It should take more studies in the future to reveal the origin of the different observations.

It is well known that E_b is influenced by not only molecular structures but also solid-state polarization effects and intermolecular electronic interactions. Meanwhile, the physical models used for E_b calculations are different based on theoretical simulation and experimental method. Therefore, the calculated E_b values presented in Table S5 are dramatically larger than that observed in the solid phase based on the temperature-dependent PL test. Despite some attempts to improve the accuracy of E_b measurement, it is worth noting that, as of now, a precise measurement of the E_b for Frenkel excitons remains elusive in this field.[63] Anyway, the consistency of the trends of the two methods implies that the rational steric hindrance and a slightly twisted main skeleton in Y-series molecules are beneficial for minimizing E_b through the construction of a denser molecular packing and delocalized pathway for charge transfer.

In order to explore the significance of acceptors with low E_b in facilitating efficient exciton dissociation and achieving high photovoltaic performance in low-driving-force OSCs, the state-of-art PM6 was selected as the donor, and OSCs with the architecture of ITO/PEDOT:PSS/active layer/PDINN/Ag were fabricated. The current–density–voltage (J–V) curves are shown in Figure 5A, and the photovoltaic parameters of the optimized devices are collected in Table 1. As the driving force is positively correlated with the HOMO energy level difference between the donor and acceptor, the driving force magnitudes for the three active layer systems are PM6:Y6 > PM6:Y-C5Ch > PM6:Y-ChC5 in order (Figure 5I). The PM6:Y6-based OSC showed a PCE of 16.7% with a J_{sc} of 26.5 mA cm^{-2}, a V_{oc} of 0.847 V, and an FF of 74.3%. Notably, the PCEs of the PM6:Y-C5Ch and PM6:Y-ChC5-based PSCs exhibit significantly enhancements to 17.4% and 19.1%, respectively. The main parameters contributing to the improved PCEs were V_{oc} and FF values, which increased from 0.847 V and 74.3% for Y6-based OSCs to 0.862 V and 76.7% for Y-C5Ch-based OSCs and further to 0.897 V and 79.4% for Y-ChC5-based OSCs. The difference in V_{oc} can be partially attributed to the varied nonradiative recombination loss in the OSCs based on PM6:Y6, PM6:Y-C5Ch, and PM6:Y-ChC5 (0.230, 0.223, and 0.200 eV) (Figure S24).[64] In addition, the changed charge carrier energy, particularly the blue-shifted absorption spectrum observed in the solid state of Y-ChC5, may also play a significant role (Figure S25). The calculated J_{sc} values derived from the external quantum efficiency response spectra of the three devices agreed well with the ones obtained from the J–V curves within a 3% error range (Figure 5B and Table 1). In addition, the PM6:Y-ChC5 exhibits highest internal quantum efficiency (IQE) response reaching 95% (Figure S16), implying that efficient internal charge transfer and sufficient absorbed photons were converted into charge carriers and then collected at the electrodes. These results indicate that using acceptor with a low E_b is advantageous in low-driving-force OSCs as it allows for higher V_{oc} without compromising exciton dissociation and sacrificing photocurrent.[38] Furthermore, we measured the photostability of the three devices, as shown in Figure S26. After 720 h of continuous illumination under LED light source (1 sun) by using maximum power point tracking method, the PM6:Y-C5Ch-based device retains 85% of its initial PCE, which is
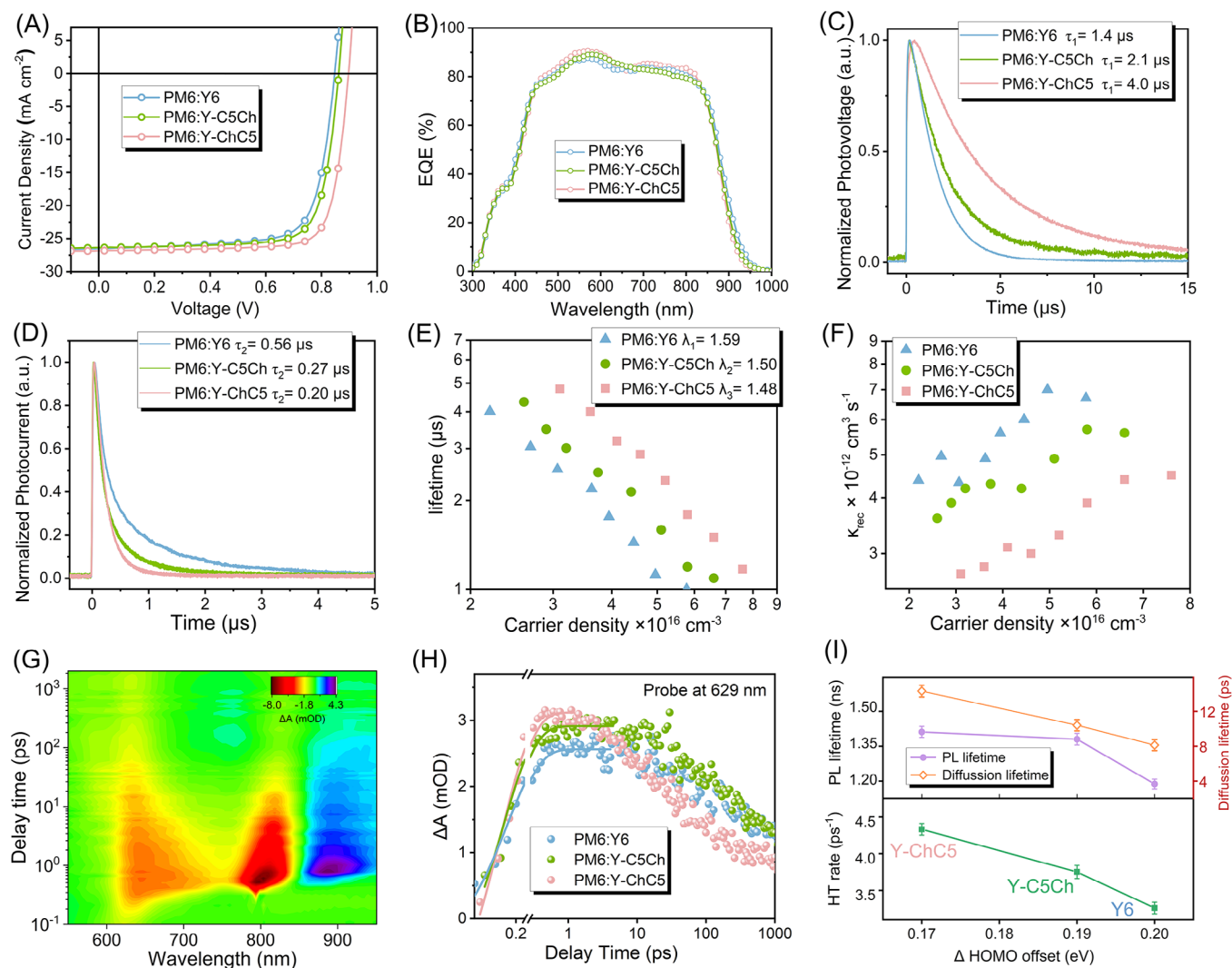
FIGURE 5 (A) J–V characteristics and (B) the related external quantum efficiency (EQE) curves for optimized devices based on PM6:Y6, PM6:Y-C5Ch, and PM6:Y-ChC5 blend films. (C) Transient photovoltage (TPV) and (D) transient photocurrent (TPC) decays of PM6:Y6, PM6:Y-C5Ch, and PM6:Y-ChC5 optimized devices. (E) Carrier lifetime versus carrier density of PM6:Y6, PM6:Y-C5Ch, and PM6:Y-ChC5 devices. (F) Bimolecular recombination rate constants (k_{rec}) versus carrier density of PM6:Y6, PM6:Y-C5Ch, and PM6:Y-ChC5 devices. (G) Two-dimensional (2D) transient absorption spectra of PM6:Y-ChC5 blend films. (H) Transient absorption (TA) kinetics of hole transfer process in PM6:Y6, PM6:Y-C5Ch, and PM6:Y-ChC5 blend films probed at 629 nm. (I) Relation graph of photoluminescence (PL) lifetimes, diffusion lifetimes, hole transfer rates, and ionization potential ("HOMO") offsets (The error bars are defined as errors originated from the instrument and data fitting). HOMO, highest occupied molecular orbital.

TABLE 1 Photovoltaic performance of the organic solar cells (OSCs) based on PM6:acceptor (1:1.2, w/w) under the illumination of AM 1.5 G, 100 Mw cm^{-2}.

Active layer	V_{oc} (V)	J_{sc} (mA cm^{-2})	$J_{cal.}$ (mA cm^{-2})[a]	FF (%)	PCE (%)
PM6:Y6	0.847	26.5	25.7	74.3	16.7 (16.4 ± 0.2)
PM6:Y-C5Ch	0.862	26.3	25.6	76.7	17.4 (17.1 ± 0.3)
PM6:Y-ChC5	0.897	26.8	26.2	79.4	19.1 (18.8 ± 0.3)

Abbreviations: EQE, external quantum efficiency; PCE, power conversion efficiency.
[a]The integrated J_{sc} from the EQE curves.

obviously higher than those of PM6:Y6- (85% after 160 h) and PM6:Y-ChC5-based device (85% after 520 h). These results revealed that the precise steric hindrance modulation of SMAs can simultaneously improve the photovoltaic performance and photostability.

To understand the reasons for different photovoltaic performances of the three SMAs, atomic force microscopy images with the contact mode of the active layers were recorded (Figure S17). As shown in Figure S17, the PM6:Y6,

PM6:Y-C5Ch, and PM6:Y-ChC5 active layers exhibit small root-mean-square roughness of 1.82, 1.64, and 1.04 nm, respectively, which is sufficiently small for forming an ohmic contact with the interface layers. Then, the miscibility among the different components of the active layer was measured via contact angle measurement. As depicted in Figure S18 and Table S6, Y-ChC5 and Y-C5Ch show better miscibility with PM6 than that of PM6:Y6 film, in favor of improving the morphology and phase separation of the active

layers.[65] Moreover, compared to PM6:Y6, PM6:Y-ChC5, and PM6:C5Ch obtain more delicate fibril network structures as shown in the phase images, indicating that the steric hindrance modulation of SMAs can precisely optimize the nanofibril size of blend film and improve the device performance.

In order to elucidate the exciton dissociation kinetics in D/A systems with varying driving force, we first conducted an analysis of the relationship between the photocurrent density (J_{ph}) and effective voltage (V_{eff}) to compare the exciton dissociation probabilities (P_{diss}) values of the three devices (Figure S19). The P_{diss} values under short-circuit conditions for Y6-, Y-C5Ch-, and Y-ChC5-based devices were determined to be 95.6%, 96.8%, and 97.2%, respectively, indicating excellent exciton dissociation and charge extraction (CE) process existed in all the devices. Transient photovoltage and transient photocurrent measurements revealed that Y-ChC5-based device had a longer carrier lifetime (τ_1) of 4.00 µs and a faster sweep-out time (τ_2) of 0.20 µs compared to the Y6- and Y-C5Ch-based devices (Figure 5C,D and Tables S7 and S8). This suggests that the Y-ChC5-based device exhibits superior exciton dissociation and suppressed charge recombination process, as evidenced by the prolonged carrier lifetime and accelerated CE capability.

Moreover, CE measurements were conducted at various illumination intensities to obtain the carrier densities (n) and thus to investigate dissociation and recombination behavior within devices (Figure S20). The evolution of τ with carrier densities for optimized devices is illustrated in Figure 5E. Notably, the τ for the Y-ChC5-based device is greater than that of the Y-C5Ch- and Y6-based one at various carrier density (n) with a minimum recombination order (λ) of 1.48, potentially stem from a higher exciton dissociation as verified in prior studies. Furthermore, such high n value can also be associated with the low carrier recombination rate in Y-ChC5-based device. Based on the above results, the bimolecular recombination rate constants (k_{rec}) were obtained according to the formula $k_{rec} = \frac{1}{(\lambda+1)n\tau}$.[60] The decrease in k_{rec} from Y6- to Y-C5Ch- and Y-ChC5-based devices, as illustrated in Figure 5F, at all given light intensities can explain the suppressed charge recombination and enhanced overall performance in Y-ChC5-based OSCs. Comparing these three acceptors, the Y-ChC5 exhibits slowest decay dynamic under open-circuit conditions (longer carrier lifetime, smallest k_{rec}), emphasizing that geometric structural modification through steric hindrance has great potential for realizing efficient charge in OSCs. Overall, our data indicates that by introducing bulky side chains as the steric hindrance to reduce the E_b of acceptor, it is possible to enable low-driving-force device systems to possess excellent exciton dissociation capability and CE probability, resulting in high photovoltaic performance.

Next, we performed femtosecond TA measurement to investigate the impact of steric hindrance of acceptors on the exciton dissociation and charge-transfer dynamics at the D/A interface. To selectively excite only acceptor, a pump beam with an exciton wavelength of 800 nm was employed to induce efficient hole transfer. The 2D color plots of TA spectra for blend films are depicted in Figure 5G and Figure S21, and representative TA kinetics traces at the selected wavelength are displayed in Figure 5H. The bleach decay process of photoexcited acceptor aligns with the rise in the GSB signal of PM6, providing evidence for the ultrafast hole transfer from acceptor to PM6. By fitting the hole transfer kinetics at 629 nm with a biexponential function, the Y6-, Y-C5Ch-, and Y-ChC5-based blends exhibited a fast component with τ_1 values of 0.30, 0.26, and 0.23 ps, respectively, and a slow component with τ_2 values of 8.13, 10.41, and 14.32 ps, respectively. A decrease in τ_1 indicates an expedited dissociation of acceptor excitons at the donor-acceptor interface, whereas the prolonged τ_2 suggests more time for exciton diffusion within acceptor phase toward the interface prior to dissociation.[66] This suggests that by reducing E_b of the acceptor through incorporation of rational steric hindrance, Y-ChC5-based devices with low driving force can still maintain sufficient exciton diffusion and rapid dissociation capabilities.

To gain a deeper understanding of the hole transfer dynamics from the acceptor excited state to the donor, we also conduct the time-resolved PL measurement for the three blend systems (Figure S22). As shown in Figure 5I, PL lifetimes increase on going from Y6-, to Y-C5Ch-, and to Y-ChC5-based active layers—a similar trend with the exciton diffusion lifetimes measured for the optimized BHJ. Meanwhile, the hole transfer rates for the three blend systems were estimated to be 3.3, 3.8, and 4.4 ps^{-1} for PM6:Y6, PM6:Y-C5Ch, and PM6:Y-ChC5 by classical Marcus electron transfer mode.[67] Therefore, the relationship between the evolution of τ_1 and τ_2 observed during hole transfer, and the PL lifetimes of acceptors indicates that prolonged exciton lifetimes have the potential to increase both exciton diffusion lengths and hole transfer times, without negatively affecting exciton dissociation and hole transfer rate at the donor-acceptor interface. Despite the smaller HOMO offset observed in the PM6:Y-ChC5 blend compared to the PM6:Y6 blend, a faster hole transfer rate was noted in the former. This suggests that the denser π–π stacking, more favorable BHJ bicontinuous network, and more delocalized electron cloud distribution resulting from precisely controlled steric hindrance can mitigate the negative impact on hole transfer rate and potentially enhance exciton dissociation and hole transfer efficiency.[68] Subsequently, PL quenching measurements were conducted to further confirm the charge-transfer efficiency. When acceptor was selected excited, the Y6-, Y-C5Ch-, and Y-ChC5-based blends exhibited hole transfer efficiencies of 93.3%, 94.1%, and 95.6%, respectively (Figure S23). These findings indicate that although the PM6/Y-ChC5 pair has weakest driving force at D/A interface, the PM6:Y-ChC5-based OSC outperforms the PM6:Y6- and PM6:Y-C5Ch-OSCs in terms of higher exciton dissociation and charge-transfer efficiency, contributing to the superior photovoltaic parameters. Therefore, modulating the intra-/intermolecular interactions of acceptor through rational steric hindrance can realize lower E_b, which can promote efficient exciton dissociation and charge transport in low-driving-force devices, and ultimately leading to high-performance OSCs.

3 | CONCLUSION

In summary, we have demonstrated an effective approach to minimizing the E_b of Y-series molecules by modulating

the intra- and intermolecular interaction. The construction of Y-series molecules with bulky side chain attached to the beta position of bithiophene units near main skeleton creates significant steric hindrance, causing distortion in the molecular structure and weakening of intramolecular interactions, limiting free rotation and movement within the molecule. On the other hand, this steric hindrance approach enhances intermolecular interactions, leading to a dense molecular stacking motif. This variation in molecular interactions strengthens molecular polarizability, promotes electronic orbital overlap between molecules, and facilitates charge transfer through delocalized pathways. The conspicuously reduced E_b obtained in Y-ChC5 with precise steric hindrance modulation can facilitate highly efficient charge separation, transport, and collection processes in low-driving-force OSCs, achieving an impressive PCE of 19.1% with an IQE of over 95% and relatively low voltage loss. Our work showcases the ingenious molecular design in minimizing the E_b to facilitate efficient charge separation at a low driving force, which is of great significance to the further development of OSCs.

AUTHOR CONTRIBUTIONS
Renqiang Yang and Xunchang Wang conceived the idea. Tianyu Hu synthesized materials, fabricated and measured the solar cell devices and grew the single crystals. Xufan Zheng and Ting Wang characterized the physical properties (UV, CV, UPS, DSC, 2D NMR). Bowen Gao performed the SCLC, TPV, TPC, and CE analysis. Jingnan Wu and Jingyi Xiong performed the DFT and MD analysis. Ming Wan conducted the GIWAXS measurement and the data analysis. Tianyu Hu and Tingting Cong conducted the TA measurement and the data analysis. Yuda Li and Aziz Saparbaev performed the PL analysis. Tianyu Hu and Xunchang Wang wrote the original draft. Renqiang Yang reviewed and edited the draft. Ergang Wang and Renqiang Yang directed and supervised the project. Xunchang Wang and Renqiang Yang provided the funding support. All authors analyzed the results and prepared the paper.

ACKNOWLEDGMENTS

CONFLICT OF INTEREST STATEMENT
The authors declare no conflicts of interest.

ORCID
Tianyu Hu https://orcid.org/0009-0003-7410-5913

REFERENCES
1. C. Yan, S. Barlow, Z. Wang, H. Yan, A. K. Y. Jen, S. R. Marder, X. Zhan, *Nat. Rev. Mater.* **2018**, *3*, 18003.
2. G. Zhang, F. R. Lin, F. Qi, T. Heumüller, A. Distler, H.-J. Egelhaaf, N. Li, P. C. Y. Chow, C. J. Brabec, A. K. Y. Jen, H.-L. Yip, *Chem. Rev.* **2022**, *122*, 14180.
3. H. Tang, Y. Liang, C. Liu, Z. Hu, Y. Deng, H. Guo, Z. Yu, A. Song, H. Zhao, D. Zhao, Y. Zhang, X. Guo, J. Pei, Y. Ma, Y. Cao, F. Huang, *Nature* **2022**, *611*, 271.
4. X. Xu, Q. Wei, Z. Zhou, H. He, J. Tian, H. L. Yip, Y. Fu, X. Lu, Y. Zhou, Y. Li, Y. Zou, *Adv. Funct. Mater.* **2023**, 2305017.
5. S. Song, K. T. Lee, C. W. Koh, H. Shin, M. Gao, H. Y. Woo, D. Vak, J. Y. Kim, *Energy Environ. Sci.* **2018**, *11*, 3248.
6. Q. Fan, R. Ma, J. Yang, J. Gao, H. Bai, W. Su, Z. Liang, Y. Wu, L. Tang, Y. Li, Q. Wu, K. Wang, L. Yan, R. Zhang, F. Gao, G. Li, W. Ma, *Angew. Chem. Int. Ed.* **2023**, *62*, e202308307.
7. X. Zhang, C. Li, L. Qin, H. Chen, J. Yu, Y. Wei, X. Liu, J. Zhang, Z. Wei, F. Gao, Q. Peng, H. Huang, *Angew. Chem. Int. Ed.* **2021**, *133*, 17861.
8. F. Liu, Y. Jiang, R. Xu, W. Su, S. Wang, Y. Zhang, K. Liu, S. Xu, W. Zhang, Y. Yi, W. Ma, X. Zhu, *Angew. Chem. Int. Ed.* **2023**, *63*, e202313791.
9. Y. Zhu, D. He, C. Wang, X. Han, Z. Liu, K. Wang, J. Zhang, X. Shen, J. Li, Y. Lin, C. Wang, Y. He, F. Zhao, *Angew. Chem. Int. Ed.* **2024**, *63*, e202316227.
10. J. Shi, K. Sun, Z. Chen, Y. Qiu, H. Liu, W. Ma, Q. Liu, Z. Ge, *Angew. Chem. Int. Ed.* **2024**, *63*, e202318360.
11. S. Li, L. Zhan, C. Sun, H. Zhu, G. Zhou, W. Yang, M. Shi, C.-Z. Li, J. Hou, Y. Li, H. Chen, *J. Am. Chem. Soc.* **2019**, *141*, 3073.
12. Y. Wang, J. Yu, R. Zhang, J. Yuan, S. Hultmark, C. E. Johnson, N. P. Gallop, B. Siegmund, D. Qian, H. Zhang, Y. Zou, M. Kemerink, A. A. Bakulin, C. Müller, K. Vandewal, X.-K. Chen, F. Gao, *Nat. Energy* **2023**, *8*, 978.
13. Y. Kan, Y. Sun, Y. Ren, Y. Xu, X. Jiang, H. Shen, L. Geng, J. Li, P. Cai, H. Xu, K. Gao, Y. Li, *Adv. Mater.* **2024**, *36*, 2312635.
14. S. M. Menke, N. A. Ran, G. C. Bazan, R. H. Friend, *Joule* **2018**, *2*, 25.
15. X. Gu, Y. Wei, N. Yu, J. Qiao, Z. Han, Q. Lin, X. Han, J. Gao, C. Li, J. Zhang, X. Hao, Z. Wei, Z. Tang, Y. Cai, X. Zhang, H. Huang, *CCS Chem.* **2023**, *5*, 2576.
16. S. Liu, J. Yuan, W. Y. Deng, M. Luo, Y. Xie, Q. B. Liang, Y. P. Zou, Z. C. He, H. B. Wu, Y. Cao, *Nat. Photon.* **2020**, *14*, 300.
17. C. Guan, C. Xiao, X. Liu, Z. Hu, R. Wang, C. Wang, C. Xie, Z. Cai, W. Li, *Angew. Chem. Int. Ed.* **2023**, *62*, e202312357.
18. X. Chen, M. Chen, J. Liang, H. Liu, X. Xie, L. Zhang, D. Ma, J. Chen, *Adv. Mater.* **2024**, *36*, 2313074.
19. S. Lai, Y. Cui, Z. Chen, X. Xia, P. Zhu, S. Shan, L. Hu, X. Lu, H. Zhu, X. Liao, Y. Chen, *Adv. Mater.* **2024**, *36*, 2313105.
20. X. Kong, C. Zhu, J. Zhang, L. Meng, S. Qin, J. Zhang, J. Li, Z. Wei, Y. Li, *Energy Environ. Sci.* **2022**, *15*, 2011.
21. Y. Shi, L. Zhu, Y. Yan, M. Xie, G. Liang, J. Qiao, J. Zhang, X. Hao, K. Lu, Z. Wei, *Adv. Energy Mater.* **2023**, *13*, 2300458.
22. D. Qian, Z. Zheng, H. Yao, W. Tress, T. R. Hopper, S. Chen, S. Li, J. Liu, S. Chen, J. Zhang, X.-K. Liu, B. Gao, L. Ouyang, Y. Jin, G. Pozina, I. A. Buyanova, W. M. Chen, O. Inganäs, V. Coropceanu, J.-L. Bredas, H. Yan, J. Hou, F. Zhang, A. A. Bakulin, F. Gao, *Nat. Mater.* **2018**, *17*, 703.
23. T. Xu, Z. Luo, R. Ma, Z. Chen, T. A. Dela Peña, H. Liu, Q. Wei, M. Li, C. E. Zhang, J. Wu, X. Lu, G. Li, C. Yang, *Angew. Chem. Int. Ed.* **2023**, *62*, e202304127.
24. T. Fritsch, J. Kurpiers, S. Roland, N. Tokmoldin, S. Shoaee, T. Ferron, B. A. Collins, S. Janietz, K. Vandewal, D. Neher, *Adv. Energy Mater.* **2022**, *12*, 2200641.
25. K. Nakano, Y. Chen, B. Xiao, W. Han, J. Huang, H. Yoshida, E. Zhou, K. Tajima, *Nat. Commun.* **2019**, *10*, 2520.
26. Y. Zhong, M. Causa, G. J. Moore, P. Krauspe, B. Xiao, F. Gunther, J. Kublitski, R. Shivhare, J. Benduhn, E. BarOr, S. Mukherjee, K. M. Yallum, J. Rehault, S. C. B. Mannsfeld, D. Neher, L. J. Richter, D. M. DeLongchamp, F. Ortmann, K. Vandewal, E. Zhou, N. Banerji, *Nat. Commun.* **2020**, *11*, 833.
27. L. Wang, C. Zhang, Z. Su, Y. Wang, W. Su, X. Man, Z. Ma, W. Zhang, C. Li, C. Yang, Z. Bo, *J. Mater. Chem. C* **2023**, *11*, 6971.
28. J. Zhang, Q. Chen, M. Li, G. Zhang, Z. Zhang, X. Deng, J. Xue, C. Zhao, C. Xiao, W. Ma, W. Li, *Adv. Mater.* **2024**, *36*, 2312805.
29. J. Yuan, Y. Zhang, L. Zhou, G. Zhang, H. Yip, T. Lau, C. Zhu, H. Peng, P. A. Johnson, M. Leclerc, Y. Cao, J. Ulanski, Y. Li, Y. Zou, *Joule* **2019**, *3*, 1140.
30. C. Li, J. Zhou, J. Song, J. Xu, H. Zhang, X. Zhang, J. Guo, L. Zhu, D. Wei, G. Han, J. Min, Y. Zhang, Z. Xie, Y. Yi, H. Yan, F. Gao, F. Liu, Y. Sun, *Nat. Energy* **2021**, *6*, 605.
31. L. Tian, C. Liu, F. Huang, *Sci. China Chem.* **2023**, *67*, 788.

32. C. Xiao, X. Wang, T. Zhong, R. Zhou, X. Zheng, Y. Liu, T. Hu, Y. Luo, F. Sun, B. Xiao, Z. Liu, C. Yang, R. Yang, *Adv. Sci.* **2023**, *10*, e2206580.

33. Y. Zhang, J. Deng, S. You, X. Huang, J. Liu, Y. Cheng, B. Huang, X. Chen, Z. Sun, C. Yang, Q. Y. Cao, F. Wu, L. Chen, *Adv. Funct. Mater.* **2023**, *34*, 2308151.

34. Z. Luo, H. Yan, C. Yang, *Acc. Mater. Res.* **2023**, *4*, 968.

35. L. Zhu, Y. Yi, Z. Wei, *J. Phys. Chem. C* **2018**, *122*, 22309.

36. H. W. Li, Z. Guan, Y. Cheng, T. Lui, Q. Yang, C. S. Lee, S. Chen, S. W. Tsang, *Adv. Electron. Mater.* **2016**, *2*, 1600200.

37. L. Perdigón-Toro, H. Zhang, A. Markina, J. Yuan, S. M. Hosseini, C. M. Wolff, G. Zuo, M. Stolterfoht, Y. Zou, F. Gao, D. Andrienko, S. Shoaee, D. Neher, *Adv. Mater.* **2020**, *32*, 1906763.

38. J. Liu, S. Chen, D. Qian, B. Gautam, G. Yang, J. Zhao, J. Bergqvist, F. Zhang, W. Ma, H. Ade, O. Inganäs, K. Gundogdu, F. Gao, H. Yan, *Nat. Energy* **2016**, *1*, 16089.

39. Q. Lin, A. Armin, R. C. R. Nagiri, P. L. Burn, P. Meredith, *Nat. Photon.* **2015**, *9*, 106.

40. J. Wu, H. Cha, T. Du, Y. Dong, W. Xu, C. T. Lin, J. R. Durrant, *Adv. Mater.* **2021**, *34*, 2101833.

41. L. Zhu, J. Zhang, Y. Guo, C. Yang, Y. Yi, Z. Wei, *Angew. Chem. Int. Ed.* **2021**, *133*, 15476.

42. T. Wang, W. Wang, Y. Cui, J. Ren, Z. Chen, J. Wang, H. Li, J. Li, J. Hou, *Adv. Funct. Mater.* **2024**, 2400729.

43. W. Gao, F. Qi, Z. Peng, F. R. Lin, K. Jiang, C. Zhong, W. Kaminsky, Z. Guan, C. S. Lee, T. J. Marks, H. Ade, A. K. Y. Jen, *Adv. Mater.* **2022**, *34*, 2202089.

44. H. Liang, X. Bi, H. Chen, T. He, Y. Lin, Y. Zhang, K. Ma, W. Feng, Z. Ma, G. Long, C. Li, B. Kan, H. Zhang, O. A. Rakitin, X. Wan, Z. Yao, Y. Chen, *Nat. Commun.* **2023**, *14*, 707.

45. Y. Chang, J. Zhang, Y. Chen, G. Chai, X. Xu, L. Yu, R. Ma, H. Yu, T. Liu, P. Liu, Q. Peng, H. Yan, *Adv. Energy Mater.* **2021**, *11*, 2100079.

46. X. Xue, K. Weng, F. Qi, Y. Zhang, Z. Wang, J. Ali, D. Wei, Y. Sun, F. Liu, M. Wan, J. Liu, L. Huo, *Adv. Energy Mater.* **2019**, *9*, 1802686.

47. Y. Li, N. Zheng, L. Yu, S. Wen, C. Gao, M. Sun, R. Yang, *Adv. Mater.* **2019**, *31*, 1807832.

48. G. Chai, Y. Chang, Z. Peng, Y. Jia, X. Zou, D. Yu, H. Yu, Y. Chen, P. Chow, K. Wong, J. Zhang, H. Ade, L Yang, C. Zhan, *Nano Energy* **2020**, *76*, 105087.

49. J. Wu, Z. Ling, L. R. Franco, S. Y. Jeong, Z. Genene, J. Mena, S. Chen, C. Chen, C. M. Araujo, C. F. N. Marchiori, J. Kimpel, X. Chang, F. H. Isikgor, Q. Chen, H. Faber, Y. Han, F. Laquai, M. Zhang, H. Y. Woo, D. Yu, T. D. Anthopoulos, E. Wang, *Angew. Chem. Int. Ed.* **2023**, *62*, e202302888.

50. B. R. Luginbuhl, P. Raval, T. Pawlak, Z. Du, T. Wang, G. Kupgan, N. Schopp, S. Chae, S. Yoon, A. Yi, H. Jung Kim, V. Coropceanu, J. L. Brédas, T. Q. Nguyen, G. N. M. Reddy, *Adv. Mater.* **2021**, *34*, 2105943.

51. Y. Bai, Z. Zhang, Q. Zhou, H. Geng, Q. Chen, S. Kim, R. Zhang, C. Zhang, B. Chang, S. Li, H. Fu, L. Xue, H. Wang, W. Li, W. Chen, M. Gao, L. Ye, Y. Zhou, Y. Ouyang, C. Zhang, F. Gao, C. Yang, Y. Li, Z. G. Zhang, *Nat. Commun.* **2023**, *14*, 2926.

52. C. Yang, Q. An, M. Jiang, X. Ma, A. Mahmood, H. Zhang, X. Zhao, H.-F. Zhi, M. H. Jee, H. Y. Woo, X. Liao, D. Deng, Z. Wei, J.-L. Wang, *Angew. Chem. Int. Ed.* **2023**, *16*, 5933.

53. X. Zheng, X. Wang, F. Sun, M. Wan, Z. Li, C. Xiao, T. Cong, T. Hu, Y. Liao, R. Yang, *Chem. Eng. J.* **2023**, *475*, 1385.

54. M. Huang, T. Hu, G. Han, C. Li, L. Zhu, J. Zhou, Z. Xie, Y. Sun, Y. Yi, *J. Phys. Chem. C* **2022**, *13*, 11065.

55. L. Zhu, Z. Tu, Y. Yi, Z. Wei, *J. Phys. Chem. Lett.* **2019**, *10*, 4888.

56. K. Jiang, J. Zhang, C. Zhong, F. R. Lin, F. Qi, Q. Li, Z. Peng, W. Kaminsky, S.-H. Jang, J. Yu, X. Deng, H. Hu, D. Shen, F. Gao, H. Ade, M. Xiao, C. Zhang, A. K. Y. Jen, *Nat. Energy* **2022**, *7*, 1076.

57. W. Zhu, A. P. Spencer, S. Mukherjee, J. M. Alzola, V. K. Sangwan, S. H. Amsterdam, S. M. Swick, L. O. Jones, M. C. Heiber, A. A. Herzing, G. Li, C. L. Stern, D. M. DeLongchamp, K. L. Kohlstedt, M. C. Hersam, G. C. Schatz, M. R. Wasielewski, L. X. Chen, A. Facchetti, T. J. Marks, *J. Am. Chem. Soc.* **2020**, *142*, 14532.

58. Z. Tu, G. Han, T. Hu, R. Duan, Y. Yi, *Chem. Mater.* **2019**, *31*, 6665.

59. L. Zhu, Z. Wei, Y. Yi, *J. Phys. Chem. C* **2022**, *126*, 14.

60. M. Huang, Y. Zeng, G. Han, Y. Yi, *J. Phys. Chem. C* **2023**, *127*, 5597.

61. X. Zhang, C. Li, J. Xu, R. Wang, J. Song, H. Zhang, Y. Li, Y.-N. Jing, S. Li, G. Wu, J. Zhou, X. Li, Y. Zhang, X. Li, J. Zhang, C. Zhang, H. Zhou, Y. Sun, Y. Zhang, *Joule* **2022**, *6*, 444.

62. X. Li, Y. Wu, S. Zhang, B. Cai, Y. Gu, J. Song, H. Zeng, *Adv. Funct. Mater.* **2016**, *26*, 2435.

63. S. Kashani, J. J. Rech, T. Liu, K. Baustert, A. Ghaffari, I. Angunawela, Y. Xiong, A. Dinku, W. You, K. Graham, H. Ade, *Adv. Energy Mater.* **2024**, *14*, 2302837.

64. A. Tang, B. Xiao, Y. Wang, F. Gao, K. Tajima, H. Bin, Z.-G. Zhang, Y. Li, Z. Wei, E. Zhou, *Adv. Funct. Mater.* **2018**, *28*, 1704507.

65. W. Zou, C. Han, X. Zhang, J. Qiao, J. Yu, H. Xu, H. Gao, Y. Sun, Y. Kan, X. Hao, G. Lu, Y. Yang, K. Gao, *Adv. Energy Mater.* **2023**, *13*, 2300784.

66. B. Liu, W. Xu, R. Ma, J. W. Lee, T. A. Dela Peña, W. Yang, B. Li, M. Li, J. Wu, Y. Wang, C. Zhang, J. Yang, J. Wang, S. Ning, Z. Wang, J. Li, H. Wang, G. Li, B. J. Kim, L. Niu, X. Guo, H. Sun, *Adv. Mater.* **2023**, *35*, 2308334.

67. C. He, Z. Chen, T. Wang, Z. Shen, Y. Li, J. Zhou, J. Yu, H. Fang, Y. Li, S. Li, X. Lu, W. Ma, F. Gao, Z. Xie, V. Coropceanu, H. Zhu, J.-L. Bredas, L. Zuo, H. Chen, *Nat. Commun.* **2022**, *13*, 2598.

68. S. Li, L. Zhan, N. Yao, X. Xia, Z. Chen, W. Yang, C. He, L. Zuo, M. Shi, H. Zhu, X. Lu, F. Zhang, H. Chen, *Nat. Commun.* **2021**, *12*, 4627.

SUPPORTING INFORMATION

Additional supporting information can be found online in the Supporting Information section at the end of this article.